

www.acsami.org Research Article

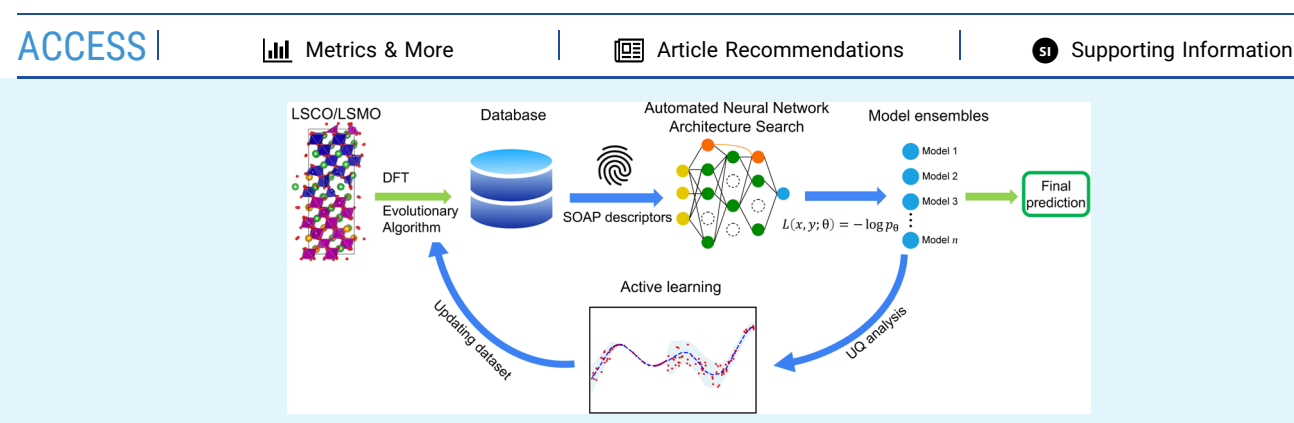
Unraveling the Correlation between the Interface Structures and Tunable Magnetic Properties of $La_{1-x}Sr_xCoO_{3-\delta}/La_{1-x}Sr_xMnO_{3-\delta}$ Bilayers Using Deep Learning Models

Hong Sun,* Vincenzo Lordi, Yayoi Takamura, and Amit Samanta*



Cite This: ACS Appl. Mater. Interfaces 2024, 16, 30166-30175





ABSTRACT: Perovskite oxides are gaining significant attention for use in next-generation magnetic and ferroelectric devices due to their exceptional charge transport properties and the opportunity to tune the charge, spin, lattice, and orbital degrees of freedom. Interfaces between perovskite oxides, exemplified by La_{1-x}Sr_xCoO_{3-δ}/La_{1-x}Sr_xMnO_{3-δ} (LSCO/LSMO) bilayers, exhibit unconventional magnetic exchange switching behavior, offering a pathway for innovative designs in perovskite oxide-based devices. However, the precise atomic-level stoichiometric compositions and chemophysical properties of these interfaces remain elusive, hindering the establishment of surrogate design principles. We leverage first-principles simulations, evolutionary algorithms, and neural network searches with on-the-fly uncertainty quantification to design deep learning model ensembles to investigate over 50,000 LSCO/LSMO bilayer structures as a function of oxygen deficiency (δ) and strontium concentration (x). Structural analysis of the low-energy interface structures reveals that preferential segregation of oxygen vacancies toward the interfacial $La_{0.7}Sr_{0.3}CoO_{3-\delta}$ layers causes distortion of the CoO_x polyhedra and the emergence of magnetically active Co^{2+} ions. At the same time, an increase in the Sr concentration and a decrease in oxygen vacancies in the $\text{La}_{0.7}\text{Sr}_{0.3}\text{MnO}_{3-\delta}$ layers tend to retain MnO_6 octahedra and promote the formation of Mn⁴⁺ ions. Electronic structure analysis reveals that the nonuniform distributions of Sr ions and oxygen vacancies on both sides of the interface can alter the local magnetization at the interface, showing a transition from ferromagnetic (FM) to local antiferromagnetic (AFM) or ferrimagnetic regions. Therefore, the exotic properties of $La_{1-x}Sr_xCoO_{3-\delta}/La_{1-x}Sr_xMnO_{3-\delta}$ are strongly coupled to the presence of hard/soft magnetic layers, as well as the FM to AFM transition at the interface, and can be tuned by changing the Sr concentration and oxygen partial pressure during growth. These insights provide valuable guidance for the precise design of perovskite oxide multilayers, enabling tailoring of their functional properties to meet specific requirements for various device applications.

KEYWORDS: perovskite oxides, exchange bias, interface design, deep learning, neural architecture search

INTRODUCTION

Perovskite oxides with tunable charge and spin states are promising materials for use in next-generation magnetic and ferroelectric devices, such as neuromorphic devices, spintronics, and magnetoelectric sensors. Interfaces between such perovskite oxides offer an added degree of freedom to tune interfacial charge transfer and magnetization switching behavior. For example, in the past few years, there has been a surge in interest in coupling two or more perovskite oxides, as La_{0.7}Sr_{0.3}CoO₃/La_{0.7}Sr_{0.3}MnO₃, La_{0.67}Sr_{0.33}MnO₃/SrRuO₃, SrRuO₃/SrMnO₃, LaNiO₃/

LaMnO₃, SrCoO₃/La_{0.7}Sr_{0.3}MnO₃, CaRuO₃/CaMnO₃, and $[Co/Pd_x]_7/CoO/[Co/Pd_y]_7$ to design exchange spring magnets, which consists of a magnetically hard material (low saturation magnetization) in contact with a magnetically soft

Received: December 14, 2023 Revised: April 18, 2024 Accepted: May 3, 2024 Published: May 23, 2024





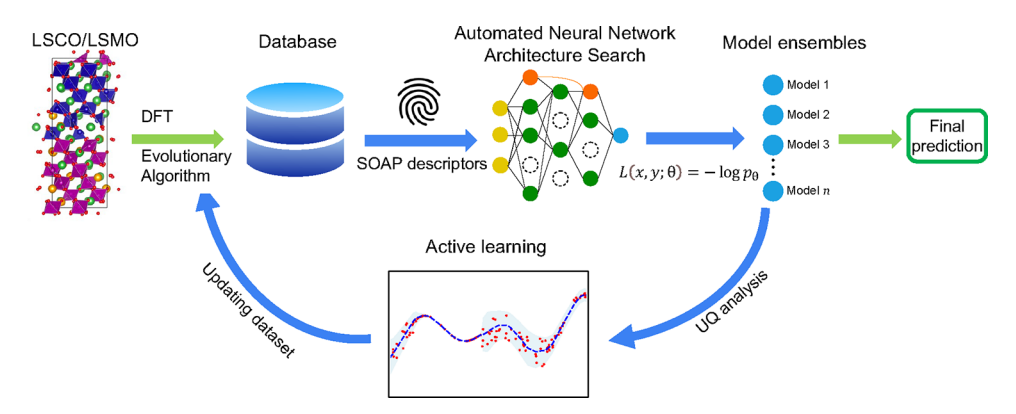


Figure 1. Schematic illustration of the interface structure search of perovskite oxides using evolutionary algorithms, automated design of deep learning models, and active learning with uncertainty quantification (UQ).

material (with high saturation magnetization) or a ferromagnetic (FM) material in contact with an antiferromagnetic (AFM) material. ¹⁶⁻¹⁸ Exchange interactions at interfaces between such materials lead to coupling between magnetic moments in the soft and hard materials and enhanced average magnetization in comparison to the hard magnetic material, thereby providing additional flexibility in designing magnets with tunable properties. In addition, it has been suggested that magnetic anisotropy can also be controlled by tailoring the distribution of oxygen vacancies in the interfacial layers, with potential applications in miniaturized high-switching speed magnetic random-access memory. ¹⁹

One such bilayer system that has attracted attention in recent years is $La_{1-x}Sr_xCoO_{3-\delta}/La_{1-x}Sr_xMnO_{3-\delta}$, which consists of bulk-like hard FM $\text{La}_{1-x}\text{Sr}_x\text{CoO}_{3-\delta}$ layers and soft FM $La_{1-x}Sr_xCoO_{3-\delta}$ layers (containing magnetically active Co^{2+}) in contact with the $La_{1-x}Sr_xMnO_{3-\delta}$ layers. Researchers have leveraged advanced experimental techniques to measure changes in magnetization, oxygen vacancy concentration, and valence states of transition metal ions at interfaces in $La_{0.7}Sr_{0.3}CoO_{3-\delta}/La_{0.7}Sr_{0.3}MnO_{3-\delta}$ bilayer systems, ^{20–22} and it has been argued that interfacial charge transfer leads to the emergence of Co²⁺ and Mn⁴⁺ ions (concluded by Kane et al.²³ from luminescence yield detection of soft X-ray magnetic spectroscopy measurements) on both sides of the interface, and that magnetically active Co²⁺ ions and oxygen vacancy concentration determine interfacial magnetization. In addition, Feng et al. have shown that magnetocrystalline anisotropy and the magnitude of exchange bias shift can be tuned by changing the thickness of the $La_{0.7}Sr_{0.3}CoO_{3-\delta}$ layers. However, in spite of the increased interest in perovskite oxide heterostructures, many questions remain unanswered: (a) Since AFM ordering has been reported in other perovskites (e.g., LaMnO₃, CaMnO₃) and also in La_{0.7}Sr_{0.3}CoO₃, is an AFM layer also present in $La_{0.7}Sr_{0.3}CoO_{3-\delta}/La_{0.7}Sr_{0.3}MnO_{3-\delta}$? (b) Is it possible to tune the Sr ions or oxygen vacancy concentration and change the magnetic behavior of this bilayer system? (c) Is there a correlation between the distribution of Sr ions and the oxygen vacancies close to the interface? (d) How does charge transfer occur between Co and Mn ions in samples with thicker $La_{0.7}Sr_{0.3}CoO_{3-\delta}$ layers? Therefore, systematic atomistic analysis is needed to fully reveal the effect of the interface structure on the physical, electronic, and magnetic properties.

Experimentally studying the effects of dopant and oxygen vacancy concentrations on the interface structure, as well as resolving the interface structure, usually requires using a

combination of multiple techniques such as transmission electron microscopy, polarized neutron reflectometry, and Xray absorption spectroscopy, which have limited availability and are time-consuming and expensive, prohibiting exploration of a large phase space of composition and structure. Similarly, the greatest obstacle in using atomistic simulations is the absence of efficient ways to sample the enormous space of possible interface structures and the distributions of dopants and oxygen vacancies. First-principles simulations using density functional theory (DFT) coupled with advanced structure searching methods, such as random structure search and evolutionary structure search, ^{29–31} have been extensively used to study structural transitions and properties of interfaces. 24-28,32-35 Since DFT calculations for systems containing lanthanides and transition metals are resource-intensive, using these automated interface structure schemes with DFT to explore interface structures at different compositions is computationally challenging and often impractical. Therefore, the lack of robust computational tools to predict probable interface structures in these complex oxides suggests that many interesting properties can be overlooked simply due to restrictive simulation capabilities and over-simplified models.

Recently, neural network-based deep learning (DL) models mapping structure to properties, e.g., total energy or structural stability, have received increasing attention as they exhibit remarkable flexibility and excellent scalability, and are computationally more efficient compared to brute force DFT calculations. 36-40 Therefore, by combining a structure search scheme with DL methods, atomic structures of interfaces and their energies (for a wide range of compositions) can be determined efficiently, and this combined scheme can remarkably accelerate the exploration of phase space and allow for screening of materials with fewer computing resources. 38-40 However, most neural network models proposed in the literature use a single neural network architecture, and this lack of model optimization, especially of neural network architecture, can induce systematic errors and lead to overfitting or underfitting issues. To mitigate this problem, we propose a framework (see Figure 1) that combines an efficient, genetic algorithm-based interface structure scheme with a state-of-the-art neural architecture search method to design ML models by optimizing neural network architectures and their hyperparameters over a wide variety of neural network ensembles. By using this prescription, we examined over 50,000 interface structures of $La_{1-x}Sr_xCoO_{3-\delta}/La_{1-x}Sr_xMnO_{3-\delta}$ bilayers across 25 distinct

compositions, spanning oxygen vacancy concentrations, $V_{\rm O}$ $(V_{\rm O} = \delta / 3)$, between 0 and 16.7% and Sr concentrations, $d_{\rm Sr}$ $(d_{Sr} = x)$, between 20.8 and 62.5%. Our in-depth analyses of the distribution of O and Sr ions, structural transformations at and away from the interface, and variations in charge and spin densities show that apart from the presence of soft and hard magnetic layers of $La_{1-x}Sr_xCoO_{3-\delta}$, small pockets of AFM domains are formed at the interface. The size of this AFM region can be controlled by changing the concentration of oxygen vacancies. This transition from FM to AFM behavior in the hard and soft magnetic layers close to the interface results in an exchange bias shift in the La_{1-x}Sr_xCoO_{3-δ}/ $La_{1-x}Sr_xMnO_{3-\delta}$ bilayers. In addition, there is preferential segregation of Sr ions on the $La_{1-x}Sr_xMnO_{3-\delta}$ side of the interface, and the Mn⁴⁺ ions in the layers close to the interface are stabilized by the cooperative arrangement of Sr ions and oxygen vacancies. On the other hand, there is a low concentration of Sr ions and a high concentration of oxygen vacancies on the $\text{La}_{1-x}\text{Sr}_x\text{CoO}_{3-\delta}$ side of the interface, which distorts the CoO6 octahedral building units and stabilizes the magnetically active Co²⁺ ions. These insights provide valuable guidance for the precise design of perovskite oxide multilayers, enabling the tailoring of their functional properties to meet specific requirements for various device applications.

METHODS

First-Principles Simulation. All supercell models of the LSCO/ LSMO bilayers are constructed in two steps. (1) We begin with the bulk structure (240 atoms) of perovskite LaCoO₃ with R3c spacegroup symmetry⁴² obtained from the Materials Project⁴³ as the template model, replacing the Co atoms located in the lower half of the LaCoO₃ structure with Mn atoms to create a LaCoO₃/LaMnO₃ bilayer. The choice of 240 atoms strikes a balance between model accuracy and computational efficiency, given the resource-intensive nature of DFT calculations. In addition, the selection of the 6-unit-cell layer thickness for each component (LSCO and LSMO) is motivated by simulation supercells adopted in various prior first-principles simulation studies of perovskite materials. 28,44–46 (2) Subsequently, we use a genetic algorithm (GA) (detailed in the Evolutionary Structure Search Using Genetic Algorithm section) to iteratively remove a fixed portion of oxygen atoms and replace a specific number of La atoms with Sr atoms to generate a wide range of La_{1-x}Sr_xCoO_{3-δ}/La_{1-x}Sr_xMnO_{3-δ} structures with distinct oxygen vacancy concentrations (V_O) and strontium concentrations (d_{Sr}) .

We conducted DFT calculations using the Vienna Ab initio Simulation Package (VASP). 47,48 To accurately account for the innercore and valence electrons, we employed the projector augmented wave (PAW)⁴⁹ method with pseudopotentials treating the following numbers of outer electrons as valence: 11 for La, 10 for Sr, 9 for Co, 7 for Mn, and 6 for O. To expand the wave functions, a plane-wave energy cutoff of 450 eV was utilized. For the exchange-correlation energy, we employed the Perdew-Burke-Ernzerhof (PBE)⁵⁰ generalized-gradient approximation (GGA) functional. During the structure optimization within the genetic algorithm, DFT calculations were performed with Gaussian smearing with a width of 0.10 eV and a 1 × 1 × 1 Monkhorst-Pack mesh for Brillouin zone integrations. Structural optimizations were performed until the forces on all atoms were below 0.05 eV/Å. Subsequently, for the analysis of the interface structure and electron and spin density distributions of the identified low-energy structures, we conducted DFT calculations using a 3×2 × 1 Monkhorst-Pack mesh, and structural optimizations were performed until the forces on all atoms were below 0.005 eV/Å.

Evolutionary Structure Search Using Genetic Algorithm. A genetic algorithm is often used as a global optimization method to optimize hyperparameters in a space of high dimensionality. Here, we employ an evolutionary algorithm to search for low-energy interface structures by mimicking the natural selection process of mutation,

crossover, and selection. 51,52 We select the distribution of the O and Sr atoms as the two structural variables and use a genetic algorithm to optimize their spatial distribution over several generations of simulations. In the first generation, 20 structures are generated by randomly removing a fixed portion of oxygen ions and replacing a certain number of La3+ ions with Sr2+ ions in a LaCoO3/LaMnO3 bilayer. These structures are optimized using first-principles simulations, and their optimized DFT energies are ranked in the ascending order. Then, 40% of the structures with lower energy and 10% of "lucky" structures by random selection are used to breed the next-generation structures by applying the crossover operation, and the offspring structures are generated by combining the structural variables of oxygen and strontium ions from each pair of parent structures. Specifically, in a child structure, the spatial distribution of oxygen vacancies is inherited from the positions of oxygen vacancies in parent A, while the distribution of strontium ions is obtained from the positions of strontium ions in parent B. This approach ensures that the offspring structures inherit the characteristics of both parents and promotes the exploration of new structural features. The mutation operation is applied to 40% of the total number of offspring structures. In the mutation operation, the spatial distribution of the oxygen vacancies and strontium ions in the selected child structures is randomized. This introduces additional diversity into the population and helps to prevent premature convergence to suboptimal solutions. The hyperparameters, including the selection rate of low-energy structures and the crossover, and mutation rates, were determined based on multiple trials to achieve a balance between the exploration of diverse offspring structures and exploiting the refinement of existing low-energy structures in each generation. The process of crossover, mutation, and selection is repeated for ~10 generations. The interface structure search for a particular composition ceases when the best fitness value (lowest energy) of each generation remains unchanged for the final two or three iterations. Note that such an evolutionary search with a stopping criterion of fewer than 10 generations is not guaranteed to find the interface structure with global minimum energy. However, the structures generated during evolutionary structure search can provide a valuable training data set to guide deep learning models in the discovery of energetically favorable structures.

Automated Design of DL Models with Uncertainty Quantification. DL models are extensively used as predictive methods for material discovery and design. The neural network models proposed in the literature are typically designed with a particular neural network architecture. The selection of hyperparameters usually involves an intensive intuition-based trial-anderror process, which is time-consuming and can induce systematic errors. Here, we employ an automated deep learning method by optimizing the network architectures and hyperparameters over a variety of neural network ensembles. We used DeepHyper, 53 an opensource AutoML package, that simultaneously performs joint neural architecture and hyperparameter searches. The performance of the neural network ensemble models is evaluated based on the uncertainty quantification. Specifically, DeepHyper uses aging evolution with Bayesian optimization (AgEBO),⁵⁴ which combines aging evolution (AgE), a parallel neural architecture search (NAS)55 method, for searching over the neural network architecture space,⁵⁶ and asynchronous Bayesian optimization (BO) for tuning the training hyperparameters. Instead of outputting a single predicted value and optimizing the parameters with the mean squared error (MSE), which is commonly adopted in regression models, we added a probabilistic neural network layer that outputs the predicted mean $\mu_{\theta}(x)$ and variance $\sigma_{\theta}(x)$ of the observed data sampled from a Gaussian distribution. The model parameters are then optimized to minimize the negative log-likelihood loss, L, as expressed in eq 1, where y is the target value (i.e., free energy) and *cst* denotes a constant value. ⁶⁰ The variance of the mean prediction of each model in the ensemble ε with K-optimized models is calculated as the epistemic uncertainty σ_u (eq 2). The performance of the neural network ensemble is evaluated by the combination of aleatoric uncertainty σ_{θ} and epistemic uncertainty σ_w expressed in eq 3.55

$$L(x, y; \theta) = -\log p_{\theta} = \frac{\log(\sigma_{\theta}^{2}(x))}{2} + \frac{(y - \mu_{\theta}(x))^{2}}{2\sigma_{\theta}^{2}(x)} + \text{cst}$$
 (1)

$$\sigma_{\mu} = \mu_{\theta} - \mu_{\varepsilon}, \ \mu_{\varepsilon} = \frac{1}{K} \sum_{\theta \in \varepsilon} \mu_{\theta} \tag{2}$$

$$\sigma_{\varepsilon}^{2} = \frac{1}{K} \sum_{\theta \in \varepsilon} \sigma_{\theta}^{2} + \frac{1}{K - 1} \sum_{\theta \in \varepsilon} \sigma_{\mu}^{2}$$
(3)

The atomic SOAP descriptor⁴¹ is used to encode the local microscopic atomic geometries using the local expansion of a Gaussian-smeared atomic density with orthonormal functions based on spherical harmonics and a radial basis function. We obtained SOAP descriptors with a dimensionality of 7380 for each structure. These descriptors were calculated using a radius cutoff of 5 Å, a maximum number of radial basis functions set to 8, and a maximum degree of spherical harmonics set to 8. Then, we applied standard scalar preprocessing to the atomic features and energy labels, which subtracted the mean of features/labels and scaled them to a unit variance between 0 and 1. To remove redundant information from the generated SOAP features, we employed principal component analysis (PCA), which is a well-known linear dimension reduction technique, to drastically reduce the dimensions of the feature space. Our analysis suggests that about 100 principal components are sufficient to encode all of the necessary information (up to an explained variance ratio of 2.70×10^{-5}).

We adopted an active learning approach to train our DL model on the fly. Specifically, we first performed automated DL with the existing DFT simulation data set. It includes 520 La_{0.7}Sr_{0.3}CoO_{3-δ}/ $La_{0.7}Sr_{0.3}MnO_{3-\delta}$ configurations obtained from an evolutionary structure search. These structures with oxygen vacancy concentrations of 0, 4, 8, 12.5, and 16.7% are optimized by first-principles simulations. An additional set of 239 training configurations are randomly generated for the LSCO/LSMO system with a combination of strontium doping concentrations of 37.5 and 50% and oxygen vacancy concentrations of 0, 4, 8, 12.5, 16.7, and 20.8%. These 759 total configurations are randomly split into training and testing data sets with a testing ratio of 33%. Then, we performed a joint neural architecture and hyperparameter search using DeepHyper and obtained an optimized DL ensemble with uncertainty quantification. We used the trained model to predict the relaxed DFT free energy of randomly generated 50,000 LSCO/LSMO interface structures, with oxygen vacancy concentrations ranging from 0 to 16.7% and strontium concentrations ranging from 20.8 to 62.5%.

We examine the aleatoric and epistemic uncertainties of the free energy predicted for each composition. Six compositions with (d_{Sr}, V_O) pairs of (20.8%,12.5%), (20.8%,16.7%), (62.5%,12.5%), (62.5%,12.5%), (20%.8,0%), and (20.8%,8%) showed large variance in uncertainty quantification after the first iteration. We employed an active learning framework to enhance model predictions and reduce uncertainty variance. Specifically, we calculated the predicted mean and uncertainty variance for the 30 low-energy structures for each of the six compositions. In each iteration, we selected 20 structures with uncertainty variances greater than 2 eV for DFT simulations, and the structures and their DFT energy values were added to the training database. After four rounds of iteratively selecting high-variance data, performing DFT simulations, updating the database, and retraining the model, the final model exhibited a median absolute error of 0.74 eV (approximately 3 meV per atom) and a root-mean-square error of 1.7 eV (around 7 meV per atom) when the energy labels of the testing structures were compared to their predicted mean energy values from the best model ensembles.

RESULTS AND DISCUSSION

Since variations in oxygen vacancies (V_O) and Sr doping (d_{Sr}) dictate changes in the structure, charge transfer, and magnetic properties of the LSCO/LSMO bilayer system, we use our trained DL models to explore the stability of over 50,000 interface structures corresponding to 25 distinct $(V_{\rm O},\,d_{\rm Sr})$ value pairs for $V_0 \in [0, 16.7\%]$ and $d_{Sr} \in [20.8, 62.5\%]$, as shown in Figure 2. The total energy of the most energetically favorable

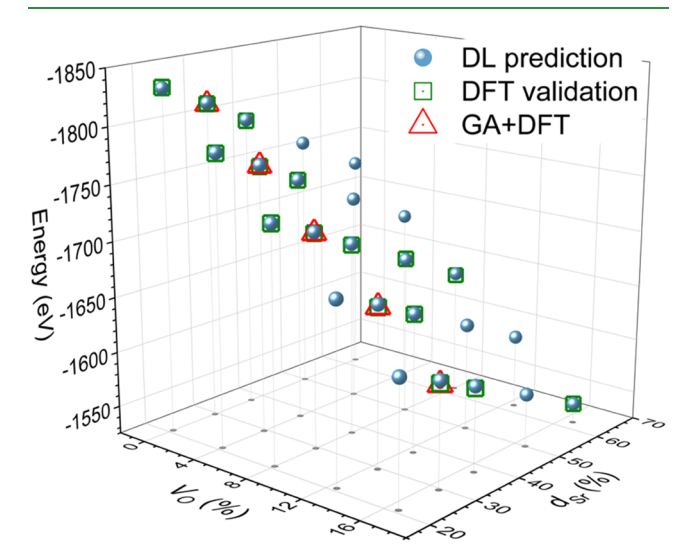


Figure 2. Free energy map of the LSCO/LSMO bilayer system as a function of oxygen vacancy concentrations (V_O) and strontium concentrations (d_{Sr}) .

interface structure identified for each (V_O, d_{Sr}) point in the two-dimensional composition space predicted by our DL models is marked by a blue sphere in Figure 2 (see SI Figure S1 for atomic configurations of three representative compositions; a detailed comparison of total energies is presented in Table S1). Due to the structural and chemical heterogeneities in this system, we validated our model predictions using two different schemes: (a) We compared the predicted lowest energy with DFT simulations at 16 randomly selected (V_0, d_{Sr}) points (out of the 25 points explored in this study), denoted by square symbols. At each of the 16 (V_O, d_{Sr}) points (marked with a square in Figure 2), DFT validation calculations were performed for the 30 most energetically favorable interface structures obtained from the DL models to check for variabilities between the model predictions and DFT. (b) Additionally, we compared the predicted lowest energy interface structures with the structures obtained from the converged evolutionary structure search, marked by triangular symbols. The agreement between DFT and evolutionary structure search confirms that DL models can reliably explore diverse sets of interface structures and predict their relative stabilities, without requiring computationally expensive DFT simulations. As shown in Table S2 in SI, the test set includes LSCO/LSMO compositions with $V_{\rm O}$ = 4%, $d_{\rm Sr}$ = 20.8% and $V_{\rm O}$ = 8%, $d_{\rm Sr}$ = 62.5%, which are absent from the compositions used in the training data sets. This demonstrates the generality of the DL model for simulating unseen LSCO/LSMO compositions.

A $La_{0.7}Sr_{0.3}CoO_{3-\delta}/La_{0.7}Sr_{0.3}MnO_{3-\delta}$ bilayer with $d_{Sr} = 30\%$ is one of the most extensively studied compositions by experiments. 20-23 We consider it as a model system to investigate the spatial distribution of oxygen vacancies and strontium ions with varying oxygen vacancies in the LSCO/ LSMO system. As illustrated in Figure 3a, our supercell model consists of thin films of LSCO and LSMO stitched together to form a bilayer system. In this interface model, significant structural changes occur in the seven middle layers across the

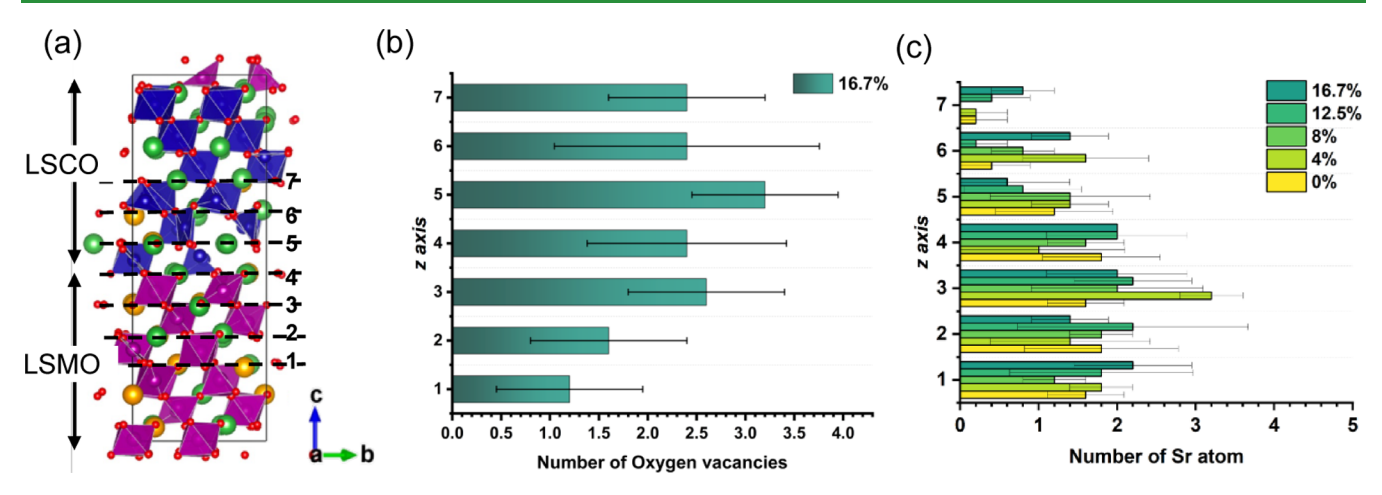


Figure 3. (a) Supercell model of the $La_{0.7}Sr_{0.3}CoO_{3-\delta}/La_{0.7}Sr_{0.3}MnO_{3-\delta}$ bilayer containing two interfacial layers. The model is viewed along the [100] direction (*a*-axis), and the [001] direction (*c*-axis) is perpendicular to the interface plane. The five elements are color-coded as follows: blue: Co, magenta: Mn, green: La, orange: Sr, and red: O. Distribution of the number of oxygen vacancies (b) and strontium ions (c) in seven labeled atomic layers (in (a)) along the *c*-axis. Different colors denote the different oxygen vacancy concentrations (V_O). Each bar represents the average value for five energetically favorable structures of each composition, and error bars denote their standard deviations.

LSCO/LSMO interface along the c-axis, as indicated in Figure 3a. We illustrate the spatial distribution of oxygen vacancies across the seven layers in LSCO/LSMO with $V_{\rm O}$ = 16.7% (Figure 3b) and $V_O = 12.5\%$ (Figure S2). Note that only the distribution of oxygen vacancies in compositions with high oxygen vacancy concentrations is presented, as the distribution of oxygen vacancies is not readily apparent in structures with small $V_{\rm O}$ (e.g., 4, 8%) due to the size limitations of the simulation model. From Figure 3b, we observe that the spatial distribution of oxygen vacancies across the LSCO/LSMO interface is heterogeneous with a higher concentration of oxygen vacancies on the LSCO side than in the LSMO layers. This preferential segregation of oxygen vacancies in the LSCO layer over the LSMO layer suggests greater tunability of oxygen vacancies and stoichiometry in LSCO. This closely aligns with experimental observations, 13-15 which reported that the oxygen vacancies in the LSCO layer could be largely tuned by ionic-liquid gating, while the stoichiometry of the LSMO layer remained unchanged. This differential modulation of the oxygen vacancy concentrations across the interface provides insights into the distinct susceptibilities of the LSCO and LSMO layers to ionic gating and highlights the potential for tailoring the properties of these complex oxide heterostructures through controlled oxygen vacancy engineering. The distribution plot of strontium ions across the seven layers in Figure 3c reveals that more strontium ions reside in the LSMO layers, especially in the region close to the interface. We acknowledge the presence of noticeable uncertainty (i.e., large deviations) due to structural disparities among energetically favorable structures. Due to the small supercells accessible in the DFT calculations, there are only a few O or Sr ions in each layer parallel to the interface. Therefore, these large errors are induced by minor deviations in the atomic densities of planes parallel to the interface, due to fluctuations in the number of O or Sr ions in a layer among the low-energy structures (identified from the genetic algorithm or DL-aided structure search). To address this deviation issue, we validated the statistical significance of the distribution results in Figure 3b,c by performing standard statistical tests. Specifically, we conducted (i) analysis of variance (ANOVA)^{57,58} and (ii) ttests, ⁵⁹ as shown in SI Table S3. Both tests yielded the same

results, indicating that the differences in the distribution of Sr ions and O vacancies between the LSCO and LSMO sides presented in Figure 3b,c are statistically significant and unlikely to have occurred by chance.

In the LSCO/LSMO bilayer with $V_{\rm O}$ = 0%, each Co and Mn ion is surrounded by six oxygen ions, forming CoO₆ and MnO₆ octahedra. The presence of oxygen vacancies leads to the transformation of CoO6 and MnO6 octahedra into distorted CoO_x and MnO_x polyhedra with a reduced number of surrounding O atoms. In the $La_{0.7}Sr_{0.3}CoO_{3-\delta}$ $La_{0.7}Sr_{0.3}MnO_{3-\delta}$ model, the higher concentration of oxygen vacancies in the LSCO layers may result in more significant structural distortion and rotation in the CoO_r octahedral polyhedra compared to the MnO_x octahedra in the LSMO layers (a detailed examination of the structural changes in the Co/MnO_x polyhedra is presented in the following paragraphs). Since Co and Mn ions have multiple valence and magnetization states,⁶¹ this heterogeneous distribution of oxygen vacancies and the accompanying structural distortion of Co/ MnO_x polyhedra also affect the valence charge of the transition metal (TM) ions.

To further understand the multivalency of Co and Mn in these bilayers, we rely on the theory of magnetism^{62,63} proposed by Goodenough and Zener, which states that double-exchange interactions may arise between TM ions with different valence states through electron hopping between the outermost orbitals of the TM ions (e_g^* orbital) and oxygen ions (2p orbital). Specifically, in the LSCO layer, Co⁴⁺ and Co³⁺ ions with low saturation magnetization coexist and their double-exchange interactions result in hard ferromagnetic coupling. 22,23 On the other hand, LSMO layers present a soft ferromagnetic coupling dominated by the exchange interaction between Mn⁴⁺ and Mn³⁺ ions with higher saturation magnetization. ^{22,23} Due to the electrostatic interactions and strong hybridization of the 3d states of Co and Mn ions with the nearest 2p orbitals of the O^{2-} ions, the valence states of Co and Mn ions in the LSCO/LSMO layers are directly related to the concentration of oxygen vacancies. As shown in Figure 3b, the preferential segregation of oxygen vacancies into layer 5 within the LSCO layers can contribute to the deoxidation of Co ions from Co⁴⁺ and Co³⁺ to Co²⁺ around the interface.

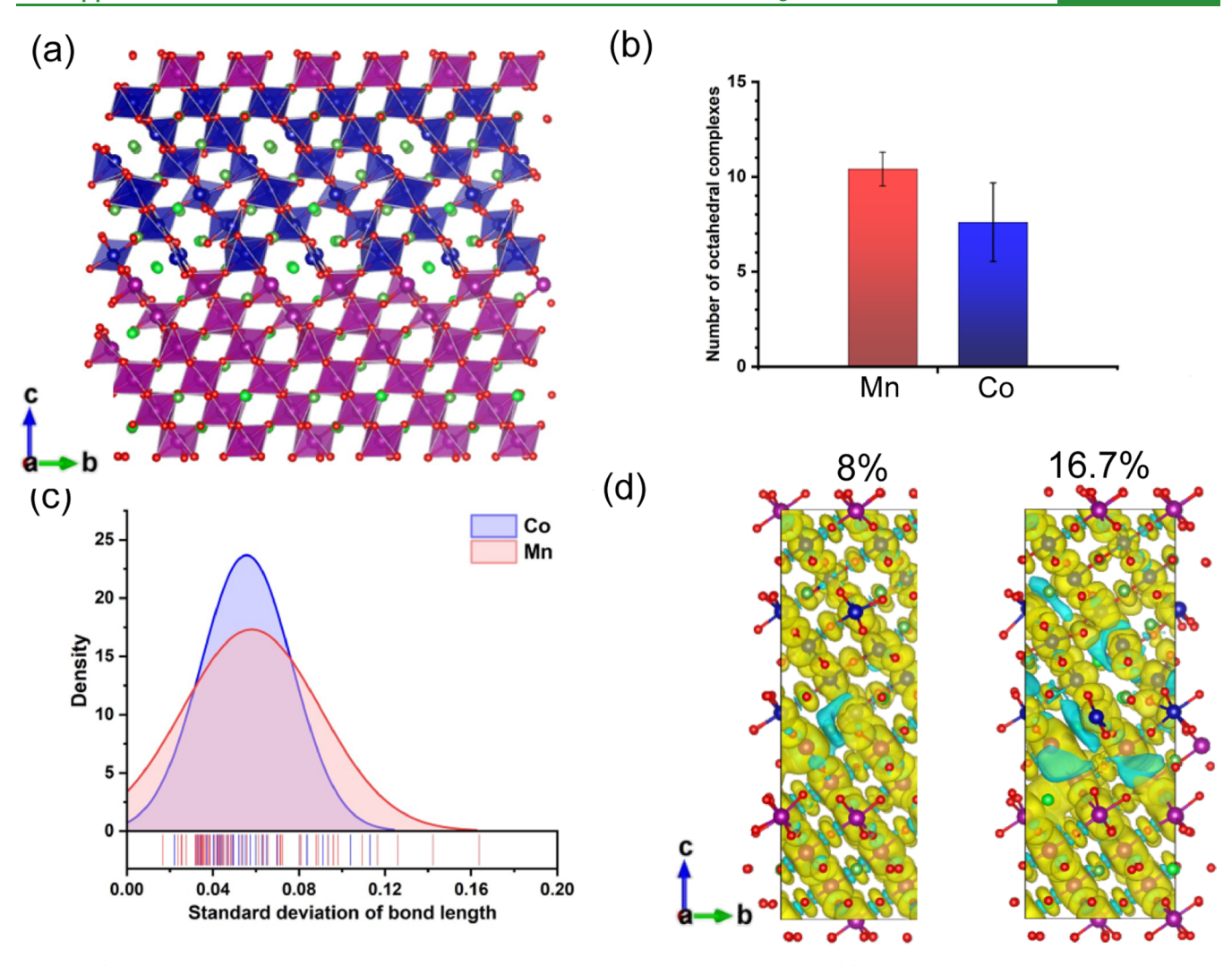


Figure 4. (a) Atomic configurations of the LSCO/LSMO supercell with $d_{\rm Sr}=30\%$ and $V_{\rm O}=16.7\%$. (b) Comparison of CoO₆ and MnO₆ octahedra counts. Error bars denote standard deviations. (c) Distribution of standard deviation of CoO and MnO bond lengths in their octahedral units. (d) Spin density isosurfaces of the LSCO/LSMO model with $V_{\rm O}=8\%$ (left) and $V_{\rm O}=16.7\%$ (right). Yellow and blue isosurfaces correspond to the spin-up and spin-down densities, respectively. The isosurface value of the spin-charge is 0.001 e/Å³.

Meanwhile, the increase of strontium ions in the LSMO layers near the interface in Figure 3c can promote the formation of Mn⁴⁺ ions, as the oxidation of Mn³⁺ to Mn⁴⁺ can compensate for the reduced positive valence caused by the substitution of Sr²⁺ ions for La³⁺ ions. We note that these observations, i.e., the change in the valence states of Co ions and the increase in the number of Mn⁴⁺ ions at the interface agree well with the recent experimental observations. This phenomenon may give rise to potential charge transfer between Co²⁺ and Mn⁴⁺ ions at the interface, consequently leading to modifications in the interfacial magnetic interactions.

Next, we analyze the relationship between the structural changes in the Co–O and Mn–O polyhedra and the local spin density distribution. In the LSCO/LSMO supercell with $d_{\rm Sr}=30\%$, with an increase in the oxygen vacancy concentration, the number of CoO₆ and MnO₆ octahedra decreases, and their structures are distorted in different ways. Here, we take the supercell of LSCO/LSMO with $V_{\rm O}=16.7\%$ as a model system to study the structural changes of CoO_x and MnO_x polyhedra due to the presence of oxygen vacancies and the atomic structure at the interface. In Figure 4a, we show the spatial distribution of CoO_x polyhedra (blue) and MnO_x polyhedra

(magenta) in the $La_{0.7}Sr_{0.3}CoO_{2.5}/La_{0.7}Sr_{0.3}MnO_{2.5}$ supercell. Generally, more structural deformations of the octahedral unit are observed in LSCO layers than in LSMO layers. The accumulation of oxygen vacancies in the LSCO layers near the interface disrupts the connections between the neighboring CoO_6 octahedra. The resulting disconnection between neighboring CoO_6 octahedra causes displacement and rotation of the CoO_x polyhedra, and one such instance is shown in Figure 4a.

In contrast to the substantial structural distortion of the ${\rm CoO}_x$ polyhedra in LSCO layers, the ${\rm MnO}_x$ polyhedra remain relatively stable and undergo minor positional and rotational adjustments within the LSMO layers. The degree of structural distortion of the ${\rm CoO}_x$ and ${\rm MnO}_x$ polyhedra can be quantitatively assessed by calculating the number of existing ${\rm CoO}_6$ and ${\rm MnO}_6$ octahedra, respectively, and by analyzing the bond length distributions of these octahedra. In Figure 4b, we plot the number of ${\rm CoO}_6$ (blue bar) and ${\rm MnO}_6$ (red bar) octahedra averaged over five energetically favorable LSCO/LSMO structures with $d_{\rm Sr}=30\%$ and $V_{\rm O}=16.7\%$. The average number of ${\rm MnO}_6$ octahedra is ~40% higher than that of ${\rm CoO}_6$ octahedra, which is consistent with the observation of

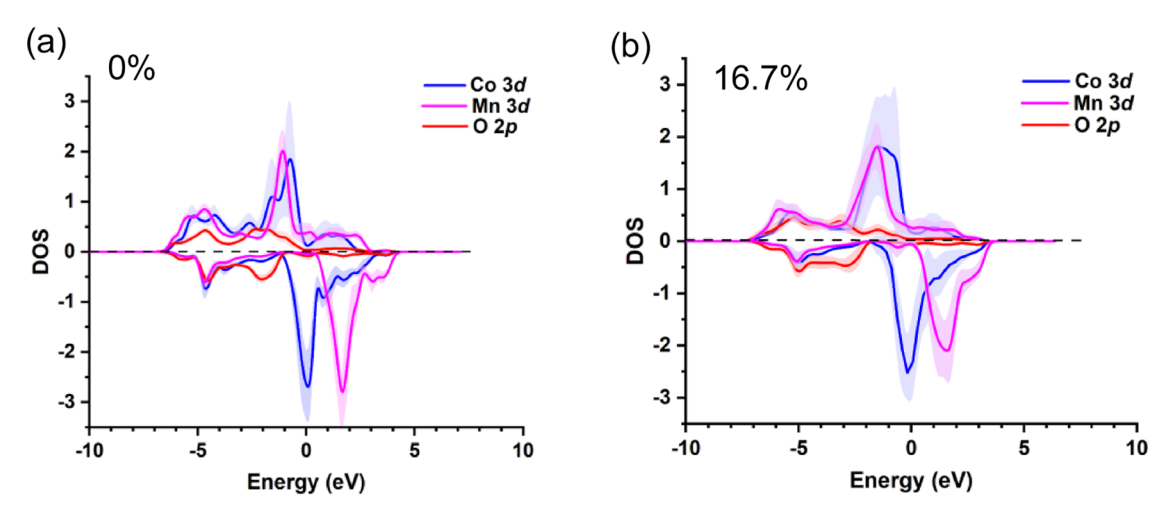


Figure 5. PDOS plots of 3d orbitals of all Co and Mn atoms and 2p orbitals of O atoms in LSCO/LSMO layers with 30% d_{Sr} , 0% V_O (a) and 30% d_{Sr} , 16.7% V_O (b). The Fermi energy is shifted to zero. Positive values represent the spin-up PDOS, while negative values denote the spin-down PDOS

preferential segregation of oxygen vacancies in the interfacial LSCO layers. The standard deviation of the bond lengths of the MnO₆ and CoO₆ octahedra shown in Figure 4c reveals that the bonding states of the MnO₆ polyhedra show larger deviations than those of the CoO₆ polyhedra. While MnO_x polyhedra undergo minor positional and rotational distortions due to the smaller concentration of oxygen vacancies, the wider range of bond lengths in the MnO_x polyhedra suggests the coexistence of distinct Mn–O bonding states within the LSMO layers. This coexistence leads to either the contraction or elongation of the bonds in one of the three 4-fold symmetrical axes of the MnO₆ octahedra. This phenomenon is also referred to as Jahn–Teller distortion.

To assess the impact of structural distortions on the magnetic characteristics of LSCO/LSMO bilayers, we perform DFT simulations with spin polarization and analyze the spin density isosurfaces of LSCO/LSMO bilayers. As shown in Figure 4d, the spin-up magnetization density (yellow) dominates the supercell, signifying a general ferromagnetic (FM) coupling. On the other hand, the appearance of small spin-down density pockets (blue) at the interface between the LSCO/LSMO layers with 8% $V_{\rm O}$ suggests the formation of localized AFM regions. As the concentration of oxygen vacancies increases to 16.7%, these AFM domains also begin to emerge within the LSCO layers. Previous studies on $La_{1-x}Sr_xCoO_{3-\delta}$ systems have also revealed a similar phenomenon, where a local AFM state was reported in FM LSCO materials and their formation was attributed to the oxygen vacancies around the Co atoms.²⁸ It is interesting to note that the local AFM states at the interfacial layers are absent in the LSCO/LSMO layers with 0% $V_{\rm O}$ (see Figure S3 in SI), which evinces the influence of oxygen vacancies in altering the local magnetization of the LSCO/LSMO bilayers. We note that there are marginal differences in the distributions of the magnetic moments of Co and Mn ions (Figure S4 in the SI) in the supercell. This can be a consequence of the small cross-section of supercells accessible in DFT simulations or a manifestation of the magnetic anisotropy and noncollinear magnetism of Mn ions. Therefore, local AFM regions (discussed above) may also manifest as local ferrimagnetic regions.

To further understand changes in the valence states and spin polarization of the Co–O and Mn–O polyhedra with different oxygen vacancy concentrations, we analyzed the spin-polarized electron density of states of two representative LSCO/LSMO compositions. According to ligand field theory, 65,67 in typical perovskite oxides, the interaction between TM ions and oxygen ligands mainly involves σ -bonding states, which result from the hybridization of the $e_{\rm g}$ level of the TM's d-orbitals with the 2p orbitals of oxygen ions. In addition, close to the Fermi level, the 3d orbitals of the TM ions become degenerate and form a $t_{\rm 2g}$ triplet $(d_{\rm xy}, d_{\rm xx})$ and $d_{\rm yz})$ that contributes to both nonbonding and antibonding states. An $e_{\rm g}^*$ doublet orbital involving $d_{\rm z2}$ and $d_{\rm x2-y2}$ orbitals contributes to the antibonding interactions. 66,67

Figure 5 shows the projected spin density of states (PDOS) of the 3d orbitals of Co and Mn, as well as the 2p orbitals of O ions, for the $La_{0.7}Sr_{0.3}CoO_3/La_{0.7}Sr_{0.3}MnO_3$ layers with 0% oxygen vacancy concentration and $La_{0.7}Sr_{0.3}CoO_{2.5}/La_{0.7}Sr_{0.3}MnO_{2.5}$ with 16.7% oxygen vacancy concentration (see SI Figures S4 and S5 for the PDOS at other compositions). The solid curves represent the average PDOS values of all respective atoms, while the shaded regions denote their standard deviations. As shown in Figure 5a,b, the significant overlap between the TM 3*d* and O 2*p* orbitals at energy levels below -4 eV (relative to the Fermi energy) points to a strong d-p hybridization for σ-bonding.

Compared to the PDOS of the pristine LSCO/LSMO system (Figure 5a), the highly oxygen-deficient LSCO/LSMO layers (Figure 5b) exhibit a broadening of the spin-up PDOS of the Co 3d orbitals within the energy range of -2 to 0 eV. Concurrently, the spin-down PDOS of the Mn 3d orbitals is broadened above the Fermi level. These broadenings signify the dispersal of the electron density around the Fermi level, indicating the emergence of mixed valence states for Co and Mn ions associated with an increase in the oxygen vacancy concentration. In the Co3+ state, the 3d orbitals are partially filled, with an electronic configuration of $3d^6$. When Co^{3+} is reduced to Co²⁺, an additional electron is incorporated into the 3d orbitals, resulting in an electronic configuration of $3d^7$. This extra electron occupies the higher energy levels of the 3d orbitals, leading to the observed broadening and shift in the peaks corresponding to the t_{2g} orbitals of the PDOS of the Co

ions toward the Fermi level. Moreover, the observed delocalization of the electron density may favor the occurrence of a double-exchange interaction across Co–O–Mn ions at the interface. Furthermore, according to ligand field theory, 65,67 the additional splitting of the $e_{\rm g}^*$ and $t_{\rm 2g}$ orbitals is associated with structural distortions within the Mn and Co octahedra. This distortion leads to heterogeneous changes in the Co–O/Mn–O bond lengths, as illustrated in Figure 4. In summary, electronic analysis provides further confirmation of the mixed oxidation states of Co/Mn atoms, the delocalization of 3d electrons, and the structural distortion of the TM-O polyhedra in the LSCO/LSMO bilayer system. Atomistic understanding provides valuable insights into the structural and compositional design strategies required to produce perovskite oxide multilayers with tunable functional properties.

CONCLUSIONS

We leveraged a novel framework that combines the automated design of deep learning models via neural architecture search with genetic algorithm-aided interface structure search to discover stable structures of ${\rm La_{1-x}Sr_xCoO_{3-\delta}/La_{1-x}Sr_xMnO_{3-\delta}}$ (LSCO/LSMO) bilayer interfaces across a wide range of compositions. Using our methodology, we successfully screened over 50,000 different interface structures for 25 compositions of LSCO/LSMO bilayers, which is not feasible via direct DFT simulations even with state-of-the-art computational resources. This method allows us to analyze the properties of the interfaces in LSCO/LSMO bilayers with unprecedented levels of sophistication and, therefore, opens new avenues to efficiently screen multicomponent materials with tunable properties for functional applications.

Structural analysis of the low-energy structures reveals nonuniform distributions of Sr ions and O vacancies that lead to different structural distortions across the interface: preferential segregation of oxygen vacancies toward interfacial $La_{0.7}Sr_{0.3}CoO_{3-\delta}$ layers causes rotational and displacive distortion of the CoO_x polyhedra and the emergence of magnetically active Co2+ ions. At the same time, an increase in strontium concentrations and a decrease in oxygen vacancies in the La_{0.7}Sr_{0.3}MnO_{3-δ} layers tend to retain MnO₆ octahedra and promote the formation of Mn⁴⁺ ions. In addition, the cooperative arrangement of strontium and oxygen vacancies leaves most MnO₆ octahedra undistorted. Electronic structure calculations reveal the delocalization of the 3d electrons of TM ions and confirms the mixed oxidation states of the Co and Mn atoms. Magnetization density calculations of the $La_{0.7}Sr_{0.3}CoO_{3-\delta}/La_{0.7}Sr_{0.3}MnO_{3-\delta}$ compositions reveal that the presence of oxygen vacancies may alter the local magnetization at the interface, showing a transition from FM to local AFM or ferrimagnetic regions. This magnetic transition is a direct consequence of the segregation behavior as well as the cooperative arrangement of strontium ions and oxygen vacancies. Therefore, the exotic properties of $La_{1-x}Sr_xCoO_{3-\delta}/La_{1-x}Sr_xMnO_{3-\delta}$ are strongly coupled to the presence of hard/soft magnetic layers as well as the FM to AFM transition at the interface.

There is a depletion of oxygen vacancies on the LSMO side of the interface, and excess oxygen vacancies are present on the LSCO side of the interface; the thickness of the soft LSCO layers can be modulated by selectively tuning the oxygen partial pressure during growth. Since oxygen vacancies significantly distort the LSCO layers close to the interface, the concentration of magnetically active Co²⁺ ions, and hence

the interfacial magnetization, can also be tuned by changing the oxygen partial pressure. Similarly, by tuning the overall Sr concentration, the amount of excess Sr ions on the LSMO side of the interface can also be varied. Consequently, both Sr and oxygen vacancies affect the width of the local AFM or ferrimagnetic region. These mechanistic details suggest structural and compositional design strategies to promote new avenues for perovskite oxide devices with tunable functional properties. Additionally, the automated design of the DL framework proposed in this work can be generally used to explore chemical structures and stability, especially for intricate multiphase models.

ASSOCIATED CONTENT

Supporting Information

The Supporting Information is available free of charge at https://pubs.acs.org/doi/10.1021/acsami.3c18773.

Supporting Information contains Table S1–S3 and Figure S1–S7 (PDF)

AUTHOR INFORMATION

Corresponding Authors

Hong Sun – Lawrence Livermore National Laboratory,
Livermore, California 94550, United States; orcid.org/
0000-0002-3586-7400; Email: sun36@llnl.gov
Amit Samanta – Lawrence Livermore National Laboratory,
Livermore, California 94550, United States; orcid.org/

Livermore, California 94550, United States; oorcid.org/ 0000-0003-3620-987X; Email: samanta1@llnl.gov

Authors

Vincenzo Lordi — Lawrence Livermore National Laboratory, Livermore, California 94550, United States; ⊙ orcid.org/ 0000-0003-2415-4656

Yayoi Takamura — Department of Materials Science and Engineering, University of California, Davis, Davis, California 95616, United States; orcid.org/0000-0002-7946-9279

Complete contact information is available at: https://pubs.acs.org/10.1021/acsami.3c18773

Notes

The authors declare no competing financial interest.

ACKNOWLEDGMENTS

This work was performed under the auspices of the U.S. Department of Energy by Lawrence Livermore National Laboratory (LLNL) under Contract DE-AC52-07NA27344. This work was funded by the Laboratory Directed Research and Development (LDRD) Program at LLNL (project tracking code 21-ERD-005). Computing support for this work was obtained from the LDRD project with tracking code 21-ERD-005. Y.T. acknowledges the support from the National Science Foundation (DMR - No. 1745450). A. S. and H. S. are grateful to Dr. Prasanna Balaprakash (Oak Ridge National Laboratory) for sharing a Jupyter notebook to set up the DeepHyper package. LLNL IM release number is LLNL-JRNL-854604.

REFERENCES

(1) Dagotto, E.; Hotta, T.; Moreo, A. Colossal Magnetoresistant Materials: The Key Role of Phase Separation. *Phys. Rep.* **2001**, 344 (1), 1–3.

- (2) Grollier, J.; Guha, S.; Ohno, H.; Schuller, I. K. Preface to Special Topic: New Physics and Materials for Neuromorphic Computation. *J. Appl. Phys.* **2018**, *124* (15), No. 151801.
- (3) Ohtomo, A.; Muller, D. A.; Grazul, J. L.; Hwang, H. Y. Artificial Charge-Modulationin Atomic-Scale Perovskite Titanate Superlattices. *Nature* **2002**, *419* (6905), 378–380.
- (4) Ohtomo, A.; Hwang, H. Y. A High-Mobility Electron Gas at the LaAlO₃/SrTiO₃ Heterointerface. *Nature* **2004**, 427 (6973), 423–426.
- (5) Feng, M.; Ahlm, N.; Sasaki, D. Y.; Chiu, I. T.; N'Diaye, A. T.; Shafer, P.; Klewe, C.; Mehta, A.; Takamura, Y. Tuning In-Plane Magnetic Anisotropy and Interfacial Exchange Coupling in Epitaxial La_{2/3}Sr_{1/3}CoO₃/La_{2/3}Sr_{1/3}MnO₃ Heterostructures. *ACS Appl. Mater. Interfaces* **2023**, *15* (45), 53086–53095.
- (6) Ke, X.; Rzchowski, M. S.; Belenky, L. J.; Eom, C. B. Positive exchange bias in ferromagnetic La_{0.67}Sr_{0.33}MnO₃/SrRuO₃ bilayers. *Appl. Phys. Lett.* **2004**, 84 (26), 5458–5460.
- (7) Padhan, P.; Prellier, W. Direct observation of pinned/biased moments in magnetic superlattices. *Phys. Rev. B* **2005**, 72 (10), No. 104416.
- (8) Padhan, P.; Prellier, W. Coercivity enhancement in the SrRuO₃/SrMnO₃ superlattices. *Appl. Phys. Lett.* **2006**, *88* (26), No. 263114.
- (9) Gibert, M.; Zubko, P.; Scherwitzl, R.; Íñiguez, J.; Triscone, J. M. Exchange bias in LaNiO₃–LaMnO₃ superlattices. *Nat. Mater.* **2012**, 11 (3), 195–198.
- (10) Ji, H.; Zhou, G.; Wang, X.; Zhang, J.; Kang, P.; Xu, X. Electric-Field Reversible Switching of the Exchange Spring and Exchange Bias Effect in SrCoO_{3-x}/La_{0.7}Sr_{0.3}MnO₃ Heterostructures. *ACS Appl. Mater. Interfaces* **2021**, *13* (13), 15774–15782.
- (11) He, C.; Grutter, A. J.; Gu, M.; Browning, N. D.; Takamura, Y.; Kirby, B. J.; Borchers, J. A.; Kim, J. W.; Fitzsimmons, M. R.; Zhai, X.; Mehta, V. V.; Wong, F. J.; Suzuki, Y. Interfacial ferromagnetism and exchange bias in CaRuO₃/CaMnO₃ superlattices. *Phys. Rev. Lett.* **2012**, *109* (19), No. 197202.
- (12) Perzanowski, M.; Zarzycki, A.; Gregor-Pawlowski, J.; Marszalek, M. (2020). Magnetization reversal mechanism in exchange-biased spring-like thin-film composite. *ACS Appl. Mater. Interfaces* **2020**, *12* (35), 39926–39934.
- (13) Cui, B.; Song, C.; Li, F.; Zhong, X. Y.; Wang, Z. C.; Werner, P.; Gu, Y. D.; Wu, H. Q.; Saleem, M. S.; Parkin, S. S. P.; Pan, F. Electric-field control of oxygen vacancies and magnetic phase transition in a cobaltite/Manganite bilayer. *Phys. Rev. Appl.* **2017**, 8 (4), No. 044007.
- (14) Song, J.; Chen, Y.; Chen, X.; Wang, H.; Khan, T.; Han, F.; Zhang, J.; Huang, H.; Zhang, J.; Zhang, H.; Zhang, H.; Yan, X.; Qi, S.; Hu, F.; Shen, B.; Yu, R.; Sun, J. Tuning the Magnetic Anisotropy of La_{2/3}Sr_{1/3}MnO₃ by Controlling the Structure of SrCoO_x in the Corresponding Bilayers Using Ionic-Liquid Gating. *Phys. Rev. Appl.* **2019**, *12* (5), No. 054016.
- (15) Song, J.; Chen, Y.; Chen, X.; Khan, T.; Han, F.; Zhang, J.; Huang, H.; Zhang, H.; Shi, W.; Qi, S.; Hu, F.; Shen, B.; Sun, J. Electric Tuning of Magnetic Anisotropy and Exchange Bias of La_{0.8}Sr_{0.2}CoO₃/La_{0.67}Sr_{0.33}MnO₃ Bilayer Films. *Phys. Rev. Appl.* **2020**, *14* (2), No. 024062.
- (16) Kneller, E. F.; Hawig, R. The exchange-spring magnet: a new material principle for permanent magnets. *IEEE Trans. Magn.* **1991**, 27 (4), 3588–3560.
- (17) Jiang, J. S.; Bader, S. D. Rational design of the exchange-spring permanent magnet. *J. Phys.: Condens. Matter* **2014**, 26 (6), No. 064214.
- (18) Fullerton, E. E.; Jiang, J. S.; Bader, S. D. Hard/soft magnetic heterostructures: model exchange-spring magnets. *J. Magn. Magn. Mater.* **1999**, 200 (1–3), 392–404.
- (19) Liao, Z.; Huijben, M.; Zhong, Z.; Gauquelin, N.; Macke, S.; Green, R. J.; Van Aert, S.; Verbeeck, J.; Van Tendeloo, G.; Held, K.; Sawatzky, G. A.; Koster, G.; Rijnders, G. Controlled lateral anisotropy in correlated Manganite heterostructures by interface-engineered oxygen octahedral coupling. *Nat. Mater.* **2016**, *15* (4), 425–431.
- (20) Li, B.; Chopdekar, R. V.; Arenholz, E.; Mehta, A.; Takamura, Y. Unconventional Switching Behavior in La_{0.7}Sr_{0.3}MnO₃/La_{0.7}Sr_{0.3}CoO₃

- Exchange-Spring Bilayers. Appl. Phys. Lett. 2014, 105 (20), No. 202401.
- (21) Li, B.; Chopdekar, R. V.; N'Diaye, A. T.; Mehta, A.; Byers, J. P.; Browning, N. D.; Arenholz, E.; Takamura, Y. Tuning Interfacial Exchange Interactions via Electronic Reconstruction in Transition-Metal Oxide Heterostructures. *Appl. Phys. Lett.* **2016**, *109* (15), No. 152401.
- (22) Kane, A. M.; Chopdekar, R. V.; N'Diaye, A. T.; Scholl, A.; Arenholz, E.; Mehta, A.; Takamura, Y. Decoupling exchange bias and coercivity enhancement in a perovskite oxide exchange spring bilayer. *Phys. Rev. Appl.* **2019**, *3* (1), No. 014413.
- (23) Kane, A. M.; Chiu, I.-T.; Ahlm, N. J.; Chopdekar, R. V.; N'Diaye, A. T.; Arenholz, E.; Mehta, A.; Lauter, V.; Takamura, Y. Controlling Magnetization Vector Depth Profiles of La_{0.7}Sr_{0.3}CoO₃/La_{0.7}Sr_{0.3}MnO₃ Exchange Spring Bilayers via Interface Reconstruction. *ACS Appl. Mater. Interfaces* **2020**, *12* (40), 45437–45443.
- (24) Jacobs, R.; Booske, J.; Morgan, D. Understanding and Controlling the Work Function of Perovskite Oxides Using Density Functional Theory. *Adv. Funct. Mater.* **2016**, 26 (30), 5471–5482.
- (25) Bennett, J. W.; Grinberg, I.; Rappe, A. M. Effect of Substituting of S for O: The Sulfide Perovskite BaZrS₃ Investigated with Density Functional Theory. *Phys. Rev. B* **2009**, *79* (23), No. 235115.
- (26) Varignon, J.; Bibes, M.; Zunger, A. Origin of Band Gaps in 3d Perovskite Oxides. *Nat. Commun.* **2019**, *10* (1), No. 1658.
- (27) Vo, H.; Zhang, S.; Wang, W.; Galli, G. Lessons Learned from First-Principles Calculations of Transition Metal Oxides. *J. Chem. Phys.* **2021**, *154* (17), No. 174704.
- (28) Zhang, S.; Galli, G. Understanding the Metal-to-Insulator Transition in $\text{La}_{1-x}\text{Sr}_x\text{CoO}_{3-\delta}$ and Its Applications for Neuromorphic Computing. *npj Comput. Mater.* **2020**, 6 (1), No. 170.
- (29) Glass, C. W.; Oganov, A. R.; Hansen, N. USPEX—Evolutionary crystal structure prediction. *Comput. Phys. Commun.* **2006**, *175* (11–12), 713–720.
- (30) Lonie, D. C.; Zurek, E. XtalOpt: An open-source evolutionary algorithm for crystal structure prediction. *Comput. Phys. Commun.* **2011**, *182* (2), 372–387.
- (31) Oganov, A. R.; Glass, C. W. Crystal structure prediction using ab initio evolutionary techniques: Principles and applications. *J. Chem. Phys.* **2006**, *124* (24), No. 244704.
- (32) Neumann, M. A.; Leusen, F. J.; Kendrick, J. A major advance in crystal structure prediction. *Angew. Chem., Int. Ed.* **2008**, 47 (13), 2427–2430.
- (33) Zhao, X.; Shu, Q.; Nguyen, M. C.; Wang, Y.; Ji, M.; Xiang, H.; Ho, K.-M.; Gong, X.; Wang, C.-Z. Interface Structure Prediction from First-Principles. *J. Phys. Chem. C* **2014**, *118* (18), 9524–9530.
- (34) Zhang, J.; Wang, C.-Z.; Ho, K.-M. Finding the Low-Energy Structures of Si[001] Symmetric Tilted Grain Boundaries with a Genetic Algorithm. *Phys. Rev. B* **2009**, *80* (17), No. 174102.
- (35) Chua, A. L.-S.; Benedek, N. A.; Chen, L.; Finnis, M. W.; Sutton, A. P. A Genetic Algorithm for Predicting the Structures of Interfaces in Multicomponent Systems. *Nat. Mater.* **2010**, *9* (5), 418–422.
- (36) Tao, Q.; Xu, P.; Li, M.; Lu, W. Machine Learning for Perovskite Materials Design and Discovery. *npj Comput. Mater.* **2021**, 7 (1), No. 23.
- (37) Talapatra, A.; Uberuaga, B. P.; Stanek, C. R.; Pilania, G. A Machine Learning Approach for the Prediction of Formability and Thermodynamic Stability of Single and Double Perovskite Oxides. *Chem. Mater.* **2021**, 33 (3), 845–858.
- (38) Zhao, J.; Wang, X. Screening Perovskites from ABO₃ Combinations Generated by Constraint Satisfaction Techniques Using Machine Learning. ACS Omega 2022, 7 (12), 10483–10491.
- (39) Li, R.; Deng, Q.; Tian, D.; Zhu, D.; Lin, B. Predicting Perovskite Performance with Multiple Machine-Learning Algorithms. *Crystals* **2021**, *11* (7), 818.
- (40) Fedorovskiy, A. E.; Queloz, V. I. E.; Nazeeruddin, M. K. Beyond Tolerance Factor: Using Deep Learning for Prediction Formability of ABX₃ Perovskite Structures. *Adv. Theory Simul.* **2021**, *4* (5), No. 2100021.

- (41) Himanen, L.; Jäger, M. O. J.; Morooka, E. V.; Federici Canova, F.; Ranawat, Y. S.; Gao, D. Z.; Rinke, P.; Foster, A. S. DScribe: Library of Descriptors for Machine Learning in Materials Science. *Comput. Phys. Commun.* **2020**, 247, No. 106949.
- (42) Nyamdavaa, E.; Altantsog, P.; Uyanga, E.; Bumaa, B.; Chen, T. Y.; Lee, C. H.; Sevjidsuren, G.; Sangaa, D. Crystal structure study of Perovskite-type LaCoO₃ electro-catalyst synthesized by Pechini method. In 6th International Forum on Strategic Technology; IEEE, 2011; pp 61–64.
- (43) Jain, A.; Ong, S. P.; Hautier, G.; Chen, W.; Richards, W. D.; Dacek, S.; Cholia, S.; Gunter, D.; Skinner, D.; Ceder, G.; Persson, K. A. Commentary: The Materials Project: A materials genome approach to accelerating materials innovation. *APL Mater.* **2013**, *1* (1), No. 011002.
- (44) Seo, M. H.; Park, H. W.; Lee, D. U.; Park, M. G.; Chen, Z. Design of highly active perovskite oxides for oxygen evolution reaction by combining experimental and ab initio studies. *ACS Catal.* **2015**, *5* (7), 4337–4344.
- (45) Jia, T.; Zeng, Z.; Lin, H. Q.; Duan, Y.; Ohodnicki, P. First-principles study on the electronic, optical and thermodynamic properties of ABO₃ (A = La, Sr, B = Fe, Co) perovskites. *RSC Adv.* **2017**, 7 (62), 38798–38804.
- (46) Akhade, S. A.; Kitchin, J. R. Effects of strain, d-band filling, and oxidation state on the surface electronic structure and reactivity of 3d perovskite surfaces. *J. Chem. Phys.* **2012**, *137* (8), No. 084703.
- (47) Kresse, G.; Joubert, D. From ultrasoft pseudopotentials to the projector augmented-wave method. *Phys. Rev. B* **1999**, *59* (3), 1758–1775.
- (48) Kresse, G.; Furthmüller, J. Efficiency of ab-initio total energy calculations for metals and semiconductors using a plane-wave basis set. *Comput. Mater. Sci.* **1996**, *6* (1), 15–50.
- (49) Blochl, P. E. Projector augmented-wave method. *Phys. Rev. B* **1994**, *50* (24), 17953.
- (50) Perdew, J. P.; Burke, K.; Ernzerhof, M. Generalized gradient approximation made simple. *Phys. Rev. Lett.* **1996**, *77* (18), 3865.
- (51) Whitley, D. A Genetic Algorithm Tutorial. Stat. Comput. 1994, 4 (2), 65–85.
- (52) Katoch, S.; Chauhan, S. S.; Kumar, V. A Review on Genetic Algorithm: Past, Present, and Future. *Multimedia Tools Appl.* **2021**, *80* (5), 8091–8126.
- (53) Balaprakash, P.; Salim, M.; Uram, T. D.; Vishwanath, V.; Wild, S. M. DeepHyper: Asynchronous Hyperparameter Search for Deep Neural Networks. In 2018 IEEE 25th International Conference on High Performance Computing (HiPC); IEEE, 2018; pp 42–51.
- (54) Égelé, R.; Balaprakash, P.; Guyon, I.; Vishwanath, V.; Xia, F.; Stevens, R.; Liu, Z. AgEBO-Tabular: Joint Neural Architecture and Hyperparameter Search with Autotuned Data-Parallel Training for Tabular Data. In SC21: International Conference for High Performance Computing, Networking, Storage and Analysis; ACM, 2021; pp 1–14.
- (55) Ginsbourger, D.; Le Riche, R.; Carraro, L. Kriging is Well-Suited to Parallelize Optimization. In *Computational Intelligence in Expensive Optimization Problems*; Springer, 2010 DOI: 10.1007/978-3-642-10701-6 6.
- (56) Caruana, R.; Niculescu-Mizil, A.; Crew, G.; Ksikes, A. *Ensemble Selection from Libraries of Models*, Proceedings of the 21st International Conference on Machine Learning; ICML, 2004; p 18.
- (57) Fisher, R. A. Statistical Methods for Research Workers (No. 5); Oliver and Boyd, 1928.
- (58) Sthle, L.; Wold, S. Analysis of variance (ANOVA). *Chemom. Intell. Lab. Syst.* **1989**, 6 (4), 259–272.
- (59) Drummond, G. B.; Tom, B. D. Statistics, probability, significance, likelihood: words mean what we define them to mean. *Adv. Physiol. Educ.* **2011**, *35* (4), *361*–*364*.
- (60) Lakshminarayanan, B.; Pritzel, A.; Blundell, C. Simple and Scalable Predictive Uncertainty Estimation Using Deep Ensembles, NIPS'17: Proceedings of the 31st International Conference on Neural Information Processing Systems; Curran Associates, Inc., 2017.
- (61) Niu, W.; Fang, Y.-W.; Zhang, X.; Weng, Y.; Chen, Y.; Zhang, H.; Gan, Y.; Yuan, X.; Zhang, S.; Sun, J.; Wang, Y.; Wei, L.; Xu, Y.;

- Wang, X.; Liu, W.; Pu, Y. Charge-Transfer-Induced Multivalent States with Resultant Emergent Magnetism in Transition-Metal Oxide Heterostructures. *Adv. Electron. Mater.* **2021**, *7* (1), No. 2000803.
- (62) Goodenough, J. B. An interpretation of the magnetic properties of the perovskite-type mixed crystals $La_{1-x}Sr_xCoO_{3-\lambda}$. J. Phys. Chem. Solids 1958, 6 (2–3), 287–297.
- (63) Zener, C. Interaction between the d-shells in the transition metals. II. Ferromagnetic compounds of manganese with perovskite structure. *Phys. Rev.* **1951**, 82 (3), 403.
- (64) Halcrow, M. A. Jahn-Teller distortions in transition metal compounds, and their importance in functional molecular and inorganic materials. *Chem. Soc. Rev.* **2013**, 42 (4), 1784–1795.
- (65) Ballhausen, C. J. Ligand Field Theory; McGraw-Hill: New York, 1962; Vol. 256.
- (66) Sun, H.; Zhao, K. Electronic structure and comparative properties of LiNi_xMn_yCo₂O₂ cathode materials. *J. Phys. Chem. C* **2017**, 121 (11), 6002–6010.
- (67) Canadell, E.; Doublet, M.-L.; Iung, C. Orbital Approach to the Electronic Structure of Solids; Oxford University Press: Oxford, U.K., 2012

■ NOTE ADDED AFTER ASAP PUBLICATION

This paper was published ASAP on May 23, 2024. Figure 1 was replaced, and the corrected version was reposted on May 29, 2024.